Progress In Electromagnetics Research B, Vol. 24, 191–221, 2010

QUALITY ASSESSMENT OF FUSED IMAGE OF MODIS AND PALSAR

G. R. Harish Kumar and D. Singh

Department of Electronics and Computer Engineering
Indian Institute of Technology Roorkee
Roorkee, India

Abstract—It is a current need of research to extensively use the freely available satellite images. The most commonly available satellite images are Moderate Resolution Imaging Spectroradiometer (MODIS) and Advanced Very High Resolution Radiometer (AVHRR). The problems with these images are their poor spatial resolution that restricts their use in various applications. This restriction may be minimized by application of the fusion techniques where high resolution image will be used to fuse with low resolution images. Another important aspect of fusion of different sensors data as optical and radar images (where both can provide the complimentary information), and the resultant fused image after fusion may give enhanced and useful information that may be beneficial for various applications. Therefore, in this paper an attempt has been made to fuse the full polarimetric Phased Array type L-band SAR (PALSAR) image with MODIS image and assess the quality of fused image. PALSAR image has a advantage of availability of data in four different channels. These four channels are HH (Transmitted horizontal polarization and received also in horizontal polarization), HV (Transmitted horizontal polarization and received vertical polarization), VH (Transmitted vertical polarization and received horizontal polarization) and VV (Transmitted vertical polarization and received vertical polarization), which provides various landcover information. The curvelet based fusion technique has been applied to MODIS Bands 1 and 2 and PALSAR (HH, HV and VV) bands for assessing the effect of fusion in land cover distinction. The three major land covers i.e., agriculture, urban and water are considered for evaluation of fusion of these images for the Roorkee area of India. The results are quite encouraging, and in near future

Received 27 February 2010, Accepted 30 June 2010, Scheduled 14 August 2010
Corresponding author: D.Singh (dharmfec@gmail.com).

it may provide a better platform for the maximize the use of MODIS images.

1. INTRODUCTION

Earth observation satellites provide data at different spatial, temporal and spectral resolutions. For the full exploitation of increasingly sophisticated multisource data, advanced analytical or numerical data fusion techniques are being developed [1, 2]. Multisource data fusion is probably the most difficult aspect in the integration of remote sensing image data products. In fact, while fusion is relatively straightforward when using data from the same satellite, the integration of imagery originating from different satellites carrying similar sensors, or even different sensors, is quite complicated.

Satellite remote sensors can be divided into two major types of imaging systems: optical and radar imaging systems. These two sensor types are very different in terms of the wavelength of their electromagnetic energy, sensor structure, and image product [3–6]. In regions with frequent cloud cover the number of suitable optical data is often limited. The all weather capability is one major advantage of radar systems with respect to optical systems. Furthermore, radar sensors provide information that is complementary to that of visible to infrared imagery. In the optical range of the electromagnetic spectrum, the information depends on reflective and emissive characteristics of the Earth's surface, whereas the radar system generates image data by recording microwave signals that are backscattered towards the antenna. Because of the differences in their data acquisition processes, image data obtained using two sensor systems often provide dissimilar and unique information over the same surface target [7]. Various Researchers [8–10] have demonstrated the benefit of combining optical and radar data for improved land cover mapping in several studies. With the availability of multifrequency and high-resolution spaceborne radar data, such as provided by the Advanced Land Observing Satellite (ALOS) Phase Array type L-Band Synthetic Aperture Radar (PALSAR) missions, an increased interest in tools to exploit the full information content of both data types is arising.

For the full exploitation of increasingly sophisticated multisource data fusion techniques are being developed. The interpretation capabilities may be enhanced by the fused images. The images used for fusion have different temporal and spatial resolution, hence a more complete view of the observed objects is provided by fused image. It is one of the main aims of image fusion to integrate different data in order to obtain more information that can be derived from each of the

single sensor data alone. A good example of this is the fusion of images acquired by different sensors having a different spatial resolution and of different spectral resolution. [1] states that the fusion of these disparate data contributes to the increasing land cover enhancement.

Researchers are applying the fusion technique since from three decades and propose various useful methods and techniques. A detailed review in the literature is given by [1]. In which some methods, like intensity-hue-saturation (IHS) [11, 12], Brovey transform [13, 14], and principal component analysis [14, 15], provide superior visual high-resolution multispectral fused images, but have a limitation of the need of high-quality spectral information as input, while these methods are useful for visual interpretation. More recently, an underlying multiresolution analysis employing the discrete wavelet transform has been used in image fusion. It was found that multisensor image fusion is a tradeoff between the spectral information from a low resolution multi-spectral images and the spatial information from a high resolution multi-spectral images. With the wavelet transform based fusion method, it is easy to control this tradeoff [16].

A high spectral quality is being provided by the wavelet-transform fusion method. However, images fused by wavelets have much less spatial information than those fused by the intensity-hue-saturation, Brovey transform, principal component analysis [17, 18]. For Land cover enhancement, the spatial information of a fused image is just as important as the spectral information. To use these information, a new transform, the curvelet transform was used in recent years by [19]. A ridgelet transform [20] is applied to square blocks of detail frames of undecimated wavelet decomposition, consequently the curvelet transform is obtained. Since the ridgelet transform possesses basis functions matching directional straight lines therefore, the curvelet transform is capable of representing piecewise linear contours on multiple scales through few significant coefficients. This property leads to a better separation between geometric details and background noise, which may be easily reduced by thresholding curvelet coefficients before they are used for fusion [19]. Therefore, the boundaries are better represented by curvelet transform than wavelets and may be well suited for extracting detailed spatial information as well as spectral information from an image, and hence, can be very useful for clustering the various targets.

The MODIS image is freely and easily available whereas PALSAR image has to be purchased. Another important aspect of MODIS image is that it is highly temporal (i.e., image is available in a couple of days). Therefore, the MODIS image may also be very useful for time series analysis. The spatial resolution of PALSAR image is 6.25 to 50 m

while as the spatial resolution of MODIS image is 250 m to 1000 m and the PALSAR image is obtained irrespective of the cloud cover. Hence in this paper, the PALSAR image is fused with the MODIS image. There is a need of research to explore the possibility of use of MODIS image for land cover enhancement with fusion techniques. Therefore, in this paper, we have attempted to explore to find the possible methodology to check the effect of fusion of MODIS and PALSAR image on land cover enhancement. For this purpose, MODIS Band 1 and Band 2 which has a special characteristics for land cover application and PALSAR (HH, HV and VV) images are being used for fusion. To critically analyze the effect of fusion we have fused MODIS Band 1 with individual channel of PALSAR images (i.e., HH, HV and VV), then MODIS Band 2 with the same bands of PALSR and after that we have fused MODIS Bands 1 and 2 image and the resultant image after this fusion is fused with individual channel of PALSAR data.

Paper contains six sections where in the second section, the study area used in this paper is discussed. In the third section, theoretical basis of the curvelet transform as well as the physical significance of the Quality Assessment indicators is explained. Implementation and results of the proposed approach are explained in the fourth section. Experimental results are dealt in the fifth section and finally the paper is concluded in the sixth section.

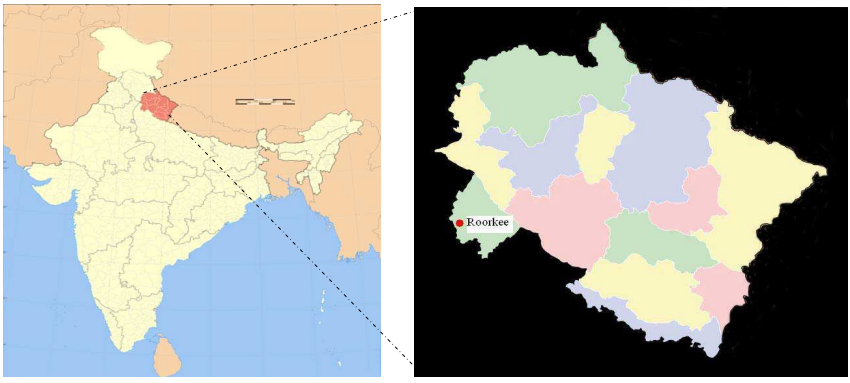

Figure 1. Location of the study area (Roorkee region) in the Haridwar district, India.

2. STUDY AREA

Roorkee Region is located in the Hardwar district of the state of Uttaranchal, India, depicted in Fig. 1, and it lies between latitudes 29°77′N and 30°N and longitudes 77°83′E and 78°01′E. The Roorkee Region has a blend of urban, water and agriculture bodies with a flat region.

2.1. Data Used

The MODIS [21] instrument provides high radiometric sensitivity (12 bit) in 36 spectral bands ranging in wavelength from 0.4 µm to 14.4 µm and also it is freely available. Two bands are imaged at a nominal resolution of 250 m at nadir, with five bands at 500 m, and the remaining 29 bands at 1 km. In this paper, the Band 1 of spatial resolution 250 m and bandwidth 620–670 nm, and Band 2, of spatial resolution of 250 m and bandwidth 842–876 nm is considered as these bands has special features to identify the agriculture and other land covers. In this paper, the MODIS image considered is MODIS/Terra Surface Reflectance 8-Day L3 Global 250 m SIN Grid (MOD09Q1). And the MODIS image is of April 7th 2009.

The Phased Array type L-band SAR (PALSAR) sensor onboard the satellite acquires SAR imagery at a wavelength of 23.5 cm (frequency 1.27 GHz) with capabilities of multimode and multipolarization observation. PALSAR can operate in several modes: the fine-beam single (FBS) polarization mode(HH), fine-beam dual (FBD) polarization mode (HH/HV or VV/VH), polarimetric (PLR) mode (HH/HV/VH/VV), and ScanSAR (WB) mode (HH/VV) (Rosenqvist et al., 2007), where HH, HV, VH and VV represent the polarizations in transmitting and receiving directions (H represents horizontal polarization and V represents vertical polarization). Depending on the different modes, PALSAR acquires image at spatial resolutions ranging from 6.25 to 50 m, with swath widths from 70 to 360 km, and off-nadir looking angles from 9.7° to 50.8° [22]. In overlapping areas, PALSAR could reach a temporal resolution higher than the satellite orbit repeat cycle of 46 days. These features, coupled with the regional observation strategy, make PALSAR imagery very attractive for spatially and temporally consistent monitoring system. In this paper, the PALSAR is of product L1.0CEOS. The PALSAR image has the incidence angle of 21.5° and approximately 30m resolution. And the PALSAR image was acquired on April 6th 2009.

The PALSAR, which is side-looking Radar will have distortion depends on terrain. As the Roorkee region is of flat region, the

PALSAR is not affected.

3. THEORETICAL BASIS

3.1. Curvelet Transform for Fusion

The main feature of the curvelet transform is that it is sensitive to directional edges and capable of representing the highpass details of object contours at different scales through few sparse nonzero coefficients. Different steps are given below for applying curvelet fusion technique.

Step 1: ATrous Wavelet Transform

The ATrous wavelet transform (ATWT) [23, 24] is a nonorthogonal multiresolution decomposition defined by a filter bank $\{h_n\}$ and $\{g_n = \delta_n - h_n\}$, with the Kronecker operator δ_n denoting an all pass filter. The filter bank does not allow perfect reconstruction to be achieved if the output is decimated. In the absence of decimation, the low pass filter is up sampled by 2^j, before processing the jth level; hence the name "ATrous" which means "with holes". In two dimensions, the filter bank becomes $\{h_m h_n\}$ and $\{\delta_m \delta_n - h_m h_n\}$ which means that the 2-D detail signals is given by the pixel difference between two successive approximations.

For J-level decomposition, the ATWT accommodates a number of coefficients $J + 1$ times greater than the number of pixels.

Due to the absence of decimation, the synthesis is simply obtained by summing details levels to the approximation:

$$f(m,n) = c_J(m,n) + \sum_{j=1}^{J} d_j(m,n) \tag{1}$$

where, $c_J(m,n)$ and $d_j(m,n)$, $j = 1, \ldots, J$ are obtained through 2-D separable linear convolution with the equivalent lowpass and highpass filters, respectively.

Step 2: Ridgelet Transform

The next step is finding a transformation capable of representing straight edges with different slopes and orientations. A possible solution is the ridgelet transform [20], which may be interpreted as the 1-D wavelet transform of the Radon transform. This is the basic idea behind the digital implementation of the ridgelet transform. The ridgelet basis function is given by [24–26]:

$$\psi_{a,b,\theta}(x_1, x_2) = a^{\frac{-1}{2}} \psi \left(\frac{(x_1 \cos\theta + x_2 \sin\theta - b)}{a} \right) \tag{2}$$

for each $a > 0$, each $b \in R$ and each $\theta \in [0, 2\pi)$. This function is constant along lines $x_1 \cos\theta + x_2 \sin\theta = \text{const}$.

Thus, the ridgelet coefficients of an image $f(x_1, x_2)$, are represented by

$$R_f(a, b, \theta) = \int_{-\infty}^{\infty} \int_{-\infty}^{\infty} \psi_{a,b,\theta}(x_1, x_2) f(x_1, x_2) dx_1 dx_2 \tag{3}$$

This transform is invertible and the reconstruction formula is given by:

$$f(x_1, x_2) = \int_{0}^{2\pi} \int_{-\infty}^{\infty} \int_{0}^{\infty} R_f(a, b, \theta) \psi_{a,b,\theta}(x_1, x_2) \frac{da}{a^3} db \frac{d\theta}{4\pi} \tag{4}$$

The Radon transform for an object f is the collection of line integrals indexed by $\theta \in [0, 2\pi) \times R$ and is given by:

$$Rf(\theta, t) = \int_{-\infty}^{\infty} \int_{-\infty}^{\infty} f(x_1, x_2) * \delta\left(x_1 \cos\theta + x_2 \sin\theta - t\right) dx_1 dx_2 \tag{5}$$

Thus, the ridgelet transform can be represented in terms of the Radon transform as follow:

$$R_f(a, b, \theta) = \int_{-\infty}^{\infty} Rf(\theta, t) a^{\frac{-1}{2}} \psi\left(\frac{(t-b)}{a}\right) dt \tag{6}$$

Hence, the ridgelet transform is the application of the 1-D wavelet transform to the slices of the Radon transform where the angular variable θ is constant and t is varying.

Step 3: Curvelet Transform

The curvelet transform is given by filtering and applying multiscale ridgelet transform on each bandpass filters which is described as following in different steps.

Step 3.1: Subband Decomposition

The image is filtered into subbands

$$f \to (P_o f, \Delta_1 f, \Delta_2 f, \ldots) \tag{7}$$

where a filter P_o deals with frequencies $\xi \leq 1$ and the bandpass filter Δ_s is concentrated near the frequencies $[2^s, 2^{2s+2}]$, e.g.,

$$\Delta_s = \psi_{2s} * f, \quad \Psi_{2s}(\xi) = \Psi\left(2^{-2s}\xi\right) \tag{8}$$

Step 3.2: Smooth Partitioning

Each subband is smoothly windowed into "squares" of an appropriate scale.

$$\Delta_s f \rightarrow (w_Q \Delta_s f)\, Q \in Q_s \tag{9}$$

Step 3.3: Renormalization

Each resulting square is renormalized to unit scale

$$g_Q = (T_Q)^{-1} (w_Q \Delta_S f), \quad Q \in Q_s \tag{10}$$

Step 3.4: Ridgelet Analysis

Each square is analyzed via the discrete ridgelet transform.

For improved visual and numerical results of the digital curvelet transform, [19] presented the following discrete curvelet transform algorithm:

i) apply the ATWT algorithm with J scales as implied in (1)

$$f(m,n) = c_J(m,n) + \sum_{j=1}^{J} d_j(m,n)$$

ii) set $B_1 = B_{\min}$;

iii) for $j = 1, \ldots j$ do
a) partition the subband w_j with a block size B_j and apply the digital ridgelet transform to each block;
b) if j modulo $2 = 1$ then $B_{j+1} = 2B_j$;
else $B_{j+1} = B_j$.

iv) Apply the ridgelet transform to each block.

Figure 2 depicts the flow chart of Curvelet Transform which explains the decomposition of the original image into subbands followed by the spatial partitioning of each subband. The Ridgelet transform is then applied to each block [19].

3.2. The Quality Assessment

In order to assess the quality of the fused product by means other than simple visual inspection of the images, some quantitative assessment criteria have been defined by comparing the fused product and the low spatial resolution multispectral images [27]. A series of indicators have been used for this purpose:

3.2.1. Correlation Coefficient

The correlation coefficient [29] of two images is often used to indicate their closeness between the images. Comparing the original image with the fused image, one can find the degree of differences. The correlation coefficient ranges from -1 to $+1$. A correlation coefficient of $+1$ indicates that the two images are highly correlated, i.e., very close to one another, and a correlation coefficient of -1 indicates that the two images are exactly opposite each other. The correlation coefficient is given by

$$corr(A,B) = \frac{\sum_{j=1}^{n}\sum_{i=1}^{m}\left(x_{i,j} - \mu(A)\right)\left(x'_{i,j} - \mu(B)\right)}{\sqrt{\sum_{j=1}^{n}\sum_{i=1}^{m}\left(x_{i,j} - \mu(A)\right)^2 \sum_{j=1}^{n}\sum_{i=1}^{m}\left(x'_{i,j} - \mu(B)\right)^2}} \tag{11}$$

where A and B are two images, $x_{i,j}$ and $x'_{i,j}$ the elements of the image A and the image B, respectively. $\mu(A)$ and $\mu(B)$ stand for their mean values. The fused image which will best preserve the spectral information of the original low resolution multispectral image is the one that has the maximum correlation with the initial low resolution multispectral image [28, 30].

3.2.2. RMSE

The Root Mean Square Error (RMSE) [31] measures the spectral fidelity between the original and the fused image. It measures the amount of change per pixel due to the processing and is described by

$$RMSE(A,B) = \sqrt{\frac{\sum_{j=1}^{n}\sum_{i=1}^{m}\left(x_{i,j} - x'_{i,j}\right)^2}{n * m}} \tag{12}$$

where A and B are two images, $x_{i,j}$ and $x'_{i,j}$ the elements of the image A and the image B, respectively.

3.2.3. RMD

The Relative Difference of Means (RMD) [30] between the fused product and the original low spatial resolution multispectral image is given by

$$RMD(F,LR) = \frac{\overline{F} - \overline{LR}}{\overline{LR}} \tag{13}$$

where $\overline{F}$ is the mean value of the fused image and $\overline{LR}$ is the mean value of the original low spatial resolution image.

The fused image which will best preserve the spectral information of the original low resolution multispectral image is the one that has the smallest possible relative difference of means.

3.2.4. RVD

The Relative Variation Difference (RVD) [30] between the fused product σ_F^2 and the original low spatial resolution multispectral image σ_{LR}^2

$$RVD(F, LR) = \frac{\sigma_F^2 - \sigma_{LR}^2}{\sigma_{LR}^2} \tag{14}$$

where $\sigma_F^2 = \frac{1}{N-1} \sum_{i=1}^{N} (F_i - \overline{F})^2$, $\sigma_{LR}^2 = \frac{1}{N-1} \sum_{i=1}^{N} (LR_i - \overline{LR})^2$.

The fused image which will best preserve the spectral information of the original low resolution multispectral image is the one that has the smallest possible relative variation difference.

3.2.5. DI

The Deviation Index (DI) [32], measuring the normalized global absolute difference of the fused image (F) with the low spatial resolution multispectral image (LR):

$$DI(F, LR) = \frac{1}{N * N} \sum_{i=1}^{N} \sum_{j=1}^{N} \frac{|F_{i,j} - LR_{i,j}|}{LR_{i,j}} \tag{15}$$

The fused image which will best preserve the spectral information of the original low resolution multispectral image is the one that has the smallest possible deviation index.

3.2.6. PSNR

The peak signal to noise ratio (PSNR) [33] index reveals the radiometric distortion of the final image compared to the original.

$$PSNR = 20 \log_{10} \frac{peak}{\sqrt{MSE}} \tag{16}$$

where

$$MSE = \frac{1}{N} \sum_{i=1}^{N} (F_i - LR_i)^2$$

where F_i is the fused image pixel i value, LR_i is the low spatial resolution image pixel i value, N is the number of non-null image pixels, Peak is the maximum possible pixel value.

The fused image which will best preserve the spectral information of the original low resolution multispectral image is the one that has the highest possible PSNR.

3.2.7. UQI

The Universal Image Quality Index (UQI) [34] introduced by

$$UQI = \frac{4\sigma_{F.LR}\overline{F}\,\overline{LR}}{\sigma_F^2 + \sigma_{LR}^2\left[\left(\overline{F}\right)^2 + \left(\overline{LR}\right)^2\right]} \tag{17}$$

where $\overline{F} = \frac{1}{N}\sum_{i=1}^{N} F_i$, $\overline{LR} = \frac{1}{N}\sum_{i=1}^{N} LR_i$, $\sigma_F^2 = \frac{1}{N-1}\sum_{i=1}^{N}(F_i - \overline{F})^2$, $\sigma_{LR}^2 = \frac{1}{N-1}\sum_{i=1}^{N}(LR_i - \overline{LR})^2$, $\sigma_{F.LR} = \frac{1}{N-1}\sum_{i=1}^{N}(F_i - \overline{F})(LR_i - \overline{LR})$. The fused image which will best preserve the spectral information of the original low resolution multispectral image is the one that has the highest possible UQI.

4. IMPLEMENTATION AND RESULTS

Figure 2 represents the basis of curvelet transform used for the fusion of PALSAR and MODIS data; whereas Figs. 3, 4 and 5 show the flowchart of the proposed methodology for the curvelet fusion of MODIS data and PALSAR data for land cover enhancement.

The raw MODIS data is initially calibrated and geo-referenced and the raw PALSAR data are also geo-referenced. Before fusing the PALSAR images, Wishart Gamma filter is applied on the PALSAR images. The Wishart Gamma Map Filter is a polarimetric filer which is suitable for polarimetric data. It performs well in the presence of regular texture and moderate relief. The filter operates under the assumption of target reciprocity (i.e., HV = VH) [35]. Hence for the PALSAR data, Wishart Gamma Map Filter is applied, and thus only three filtered images are produced (HH, HV and VV). Consequently MODIS and PALSAR data are subsetted to Roorkee region and the care is taken so that area of sub-set region of both satellite images should be approximately equal. Therefore, MODIS has $108 * 108$ pixels and PALSAR has $1071 * 1071$ no of pixels after subsetting, by which both are acquiring approximately the same area. The Subsetted MODIS Band 1 and Band 2 are shown in Figs. 8(a) and 8(b) respectively and

the subsetted PALSAR HH, HV and VV Polarized images are shown in Figs. 7(a), 7(b) and 7(c) respectively.

Fusion of MODIS Band 1 on MODIS Band 2

MODIS Band 1 and Band 2 are considered initially. The Band 1 is fused with the Band 2, through the curvelet transform Fig. 2. (For ATWT transform, (1) is computed for Band 2, thereby Band 2 is decomposed into $J + 1$ subbands, which includes C_J & d_j, where C_J is a coarse or smooth version of Band 2, and d_j is the details of Band 2 at scale 2^{-j}, here $j = 2$. C_J is replaced by Band 1 and then the Ridgelets transform ((2) to (6)) is applied to all the decomposed subbands, i.e., d_j bands, thereby obtained ridgelet coefficients are hard-thresholded in order to enhance edges in the fused image and inverse ridgelet transforms (IRT) is carried out to obtain a new image which

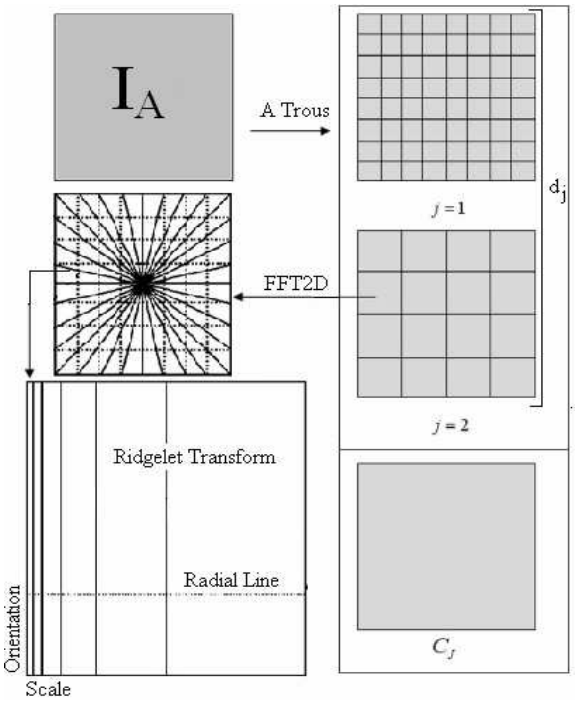

Figure 2. Curvelet transform flowgraph. The figure illustrates the decomposition of the original image into subbands followed by the spatial partitioning of each subband (i.e., each subband is decomposed into blocks). The ridgelet transform is then applied to each block [28].

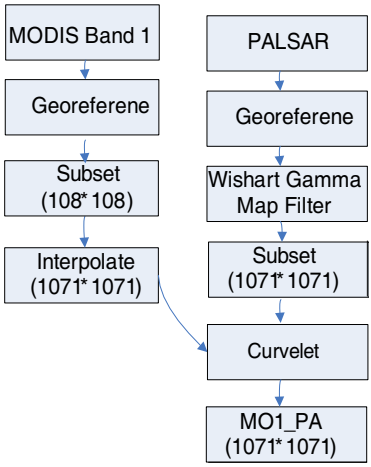

Figure 3. Flowchart the methodology, for the fusion of MODIS (Band 1) on PALSAR data.

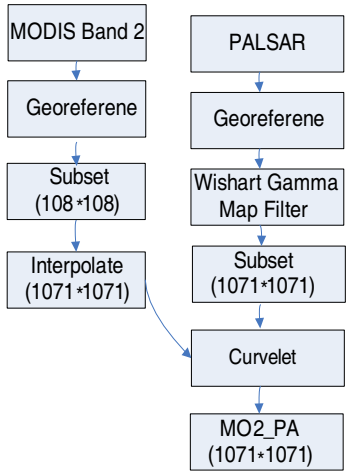

Figure 4. Flowchart the methodology, for the fusion of MODIS (Band 2) on PALSAR data.

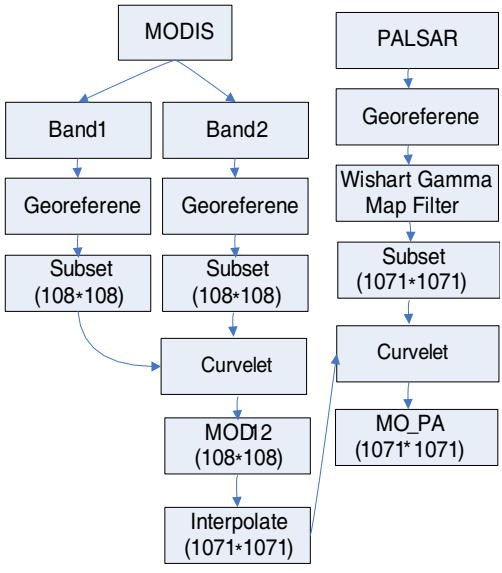

Figure 5. Flowchart the methodology, for the fusion of MODIS (Band 1 and Band 2) on PALSAR data.

reflects the fused image (MOD12) of Band 1 and Band 2, i.e., the resultant fused image MOD12 of $108 * 108$ pixels. The flowchart is depicted in Fig. 5. This MOD12 image is interpolated through bi-linear interpolation technique to the scale of the PALSAR data of $1071 * 1071$ pixels. The fused image is shown in Fig. 11(a). The flowcharts for the fusion of PALSAR images with the MODIS images are deciphered in the following steps.

Step 1: Fusion of MODIS Band 1 with the PALSAR polarized images

Figure 3 implies the proposed methodology for the fusion of MODIS Band 1 and PALSAR polarized image. MODIS Band 1 and PALSAR polarized image are considered initially and MODIS Band 1 is interpolated through bi-linear interpolation technique to the scale of the PALSAR data of 1071*1071 pixels. ATWT transformation is applied for PALSAR and C_J ($j = 3$ for present case) is replaced by MODIS Band 1 which gives the resultant fused image MO1_PA that has $1071 * 1071$ pixels. The PALSAR polarized HH band is fused with the MODIS Band 1 and the resultant fused is MO1_PA(HH) and is revealed in Fig. 9(a). Similarly the fused image of PALSAR polarized HV band is MO1_PA(HV) and is depicted in Fig. 9(b) and the fused image of PALSAR polarized VV band is MO1_PA(VV) and is shown in Fig. 9(c).

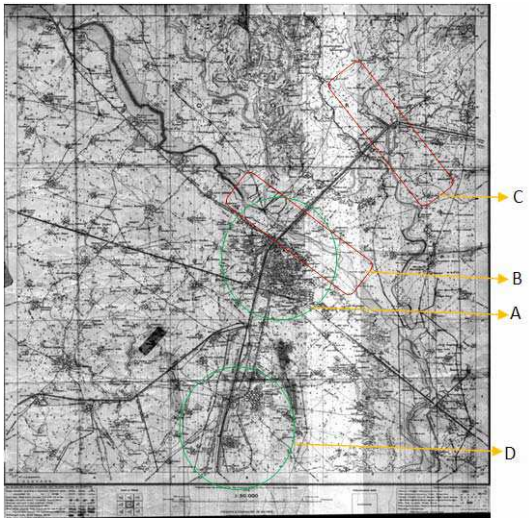

Figure 6. Toposheet of the study area (Roorkee region) in the Haridwar district, India.

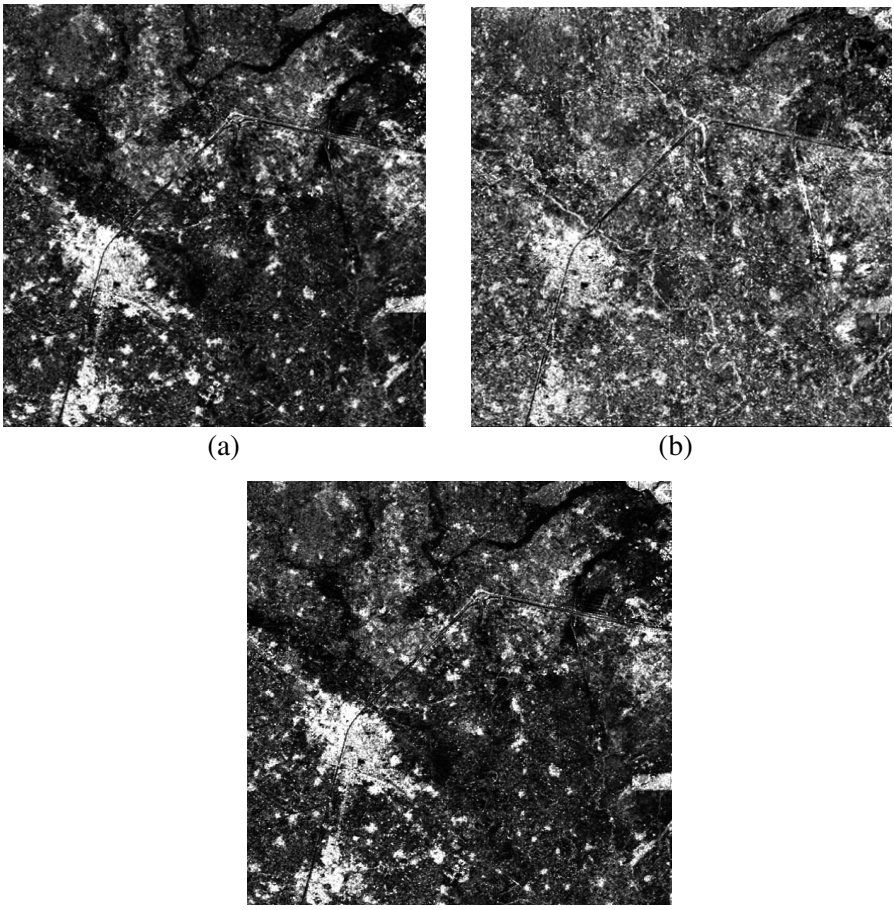

(a) (b)

(c)

Figure 7. (a) PALSAR HH polarized. (b) PALSAR HV polarized. (c) PALSAR VV polarized.

Step 2: Fusion of MODIS Band 2 with the PALSAR polarized images

The proposed methodology for the fusion of MODIS Band 2 and PALSAR polarized image is shown in Fig. 4. MODIS Band 2 and PALSAR polarized image are considered initially and MODIS Band 2 is interpolated through bi-linear interpolation technique to the scale of the PALSAR data of $1071 * 1071$ pixels. ATWT transformation is applied for all the PALSAR polarized bands and C_J ($j = 3$ for present case) is replaced by MODIS Band 2 which gives the resultant fused

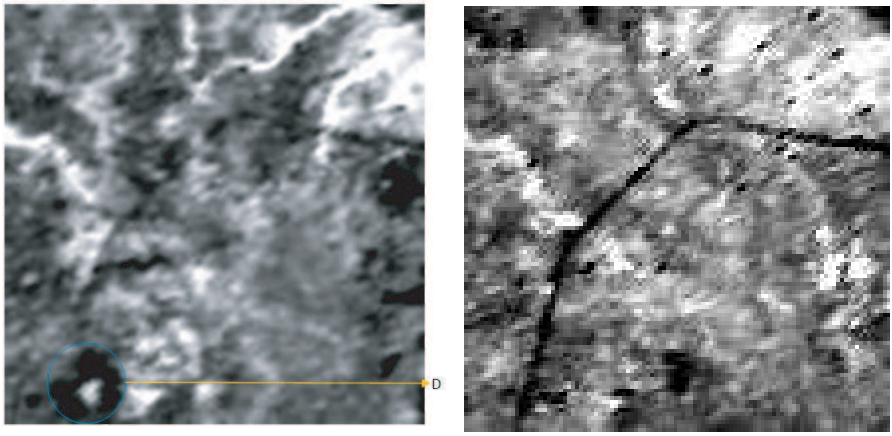

(a) (b)

Figure 8. (a) MODIS Band 1. (b) MODIS Band 2.

image MO2_PA that has $1071 * 1071$ pixels. The PALSAR polarized HH band is fused with the MODIS Band 2 and the resultant fused is MO2_PA(HH) and is revealed in Fig. 10(a). Similarly the fused image of PALSAR polarized HV band is MO2_PA(HV) and is depicted in Fig. 10(b) and the fused image of PALSAR polarized VV band is MO2_PA(VV) and is shown in Fig. 10(c).

Step 3: Fusion of MOD12 image with the PALSAR polarized images

In the flowchart of Fig. 5, the MOD12, the interpolated fused image of MODIS bands and PALSAR polarized bands are considered for the fusion. ATWT transformation is applied for all the PALSAR polarized bands and C_J ($j = 3$ for present case) is replaced by MOD12 which gives the resultant fused image MO_PA that has $1071 * 1071$ pixels. The PALSAR polarized HH band is fused with the MOD12 and the resultant fused is MO_PA(HH) and is revealed in Fig. 11(b). Similarly the fused image of PALSAR polarized HV band is MO12_PA(HV) and is depicted in Fig. 11(c) and the fused image of PALSAR polarized VV band is MO12_PA(VV) and is shown in Fig. 11(d).

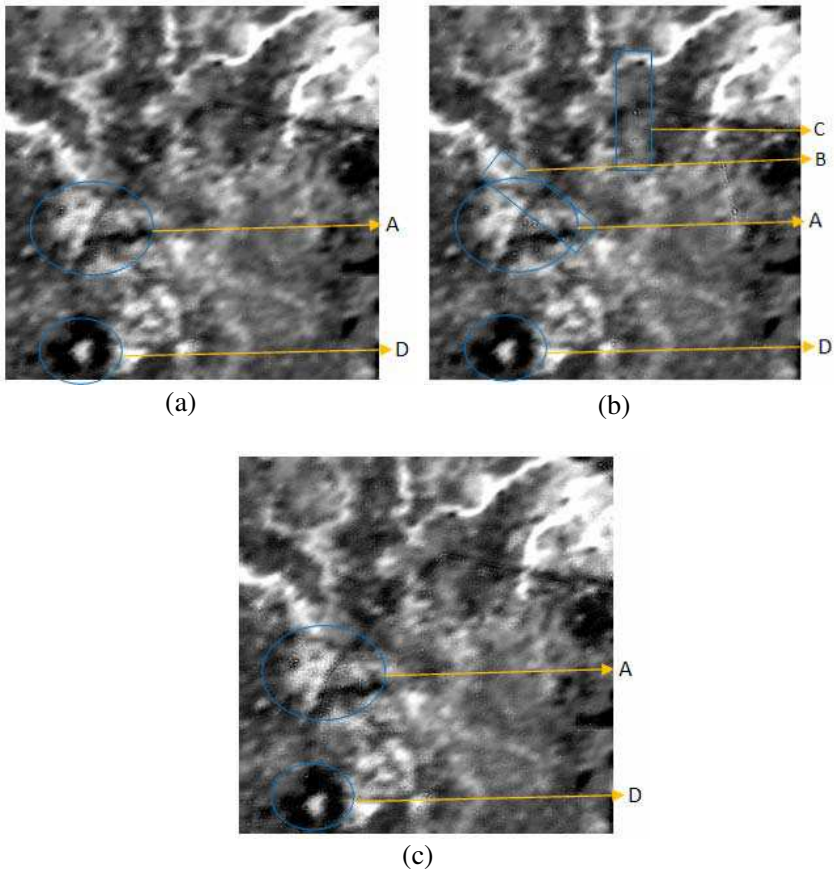

Figure 9. (a) MO1_PA(HH), the resultant fused image of MODIS Band 1and HV polarized image. (b) MO1_PA(HV), the resultant fused image of MODIS Band 1 and HH polarized image. (c) MO1_PA(VV), the resultant fused image of MODIS Band 1 and VV polarized image.

5. ANALYSIS OF EXPERIMENT RESULTS

5.1. Visual Interpretation

The toposheet for the Roorkee region is shown in Fig. 6, and on the toposheet, 4 regions are selected and it is named by A, B, C and D respectively. Region A and D are urban region, B and C are river channels. In MODIS Band 1, Fig. 8(a), only the region D can be seen and in MODIS Band 2, Fig. 8(b), none of the regions can be seen clearly.

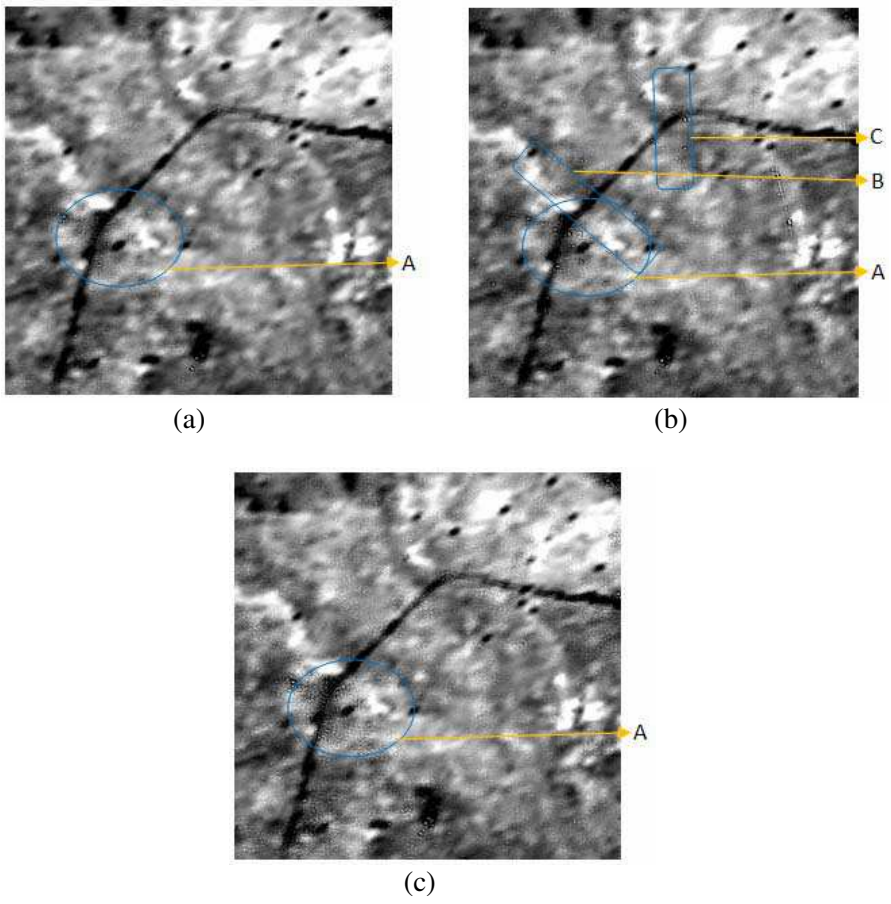

Figure 10. (a) MO2_PA(HH), the resultant fused image of MODIS Band 2 and HH polarized image. (b) MO2_PA(HV), the resultant fused image of MODIS Band 2 and HV polarized image. (c) MO2_PA(VV), the resultant fused image of MODIS Band 2 and VV polarized image.

Where as, the MODIS bands (Band 1, Band 2, and MOD12) fused with the HV PALSAR bands, i.e., MO1_PA(HV), MO2_PA(HV) and MO_PA(HV) have a distinguish river channels, i.e., the region represented by B and C are represented more clearly, and it is marked by B and C in respective Figs. 9(b), 10(b) and 11(c). The region represented by A is urban and it is clearly shown in all the fused images, i.e., MO1_PA(HH), MO1_PA(HV), MO1_PA(VV), MO2_PA(HH), MO2_PA(HV), MO2_PA(VV), MO_PA(HH), MO_PA(HV) and

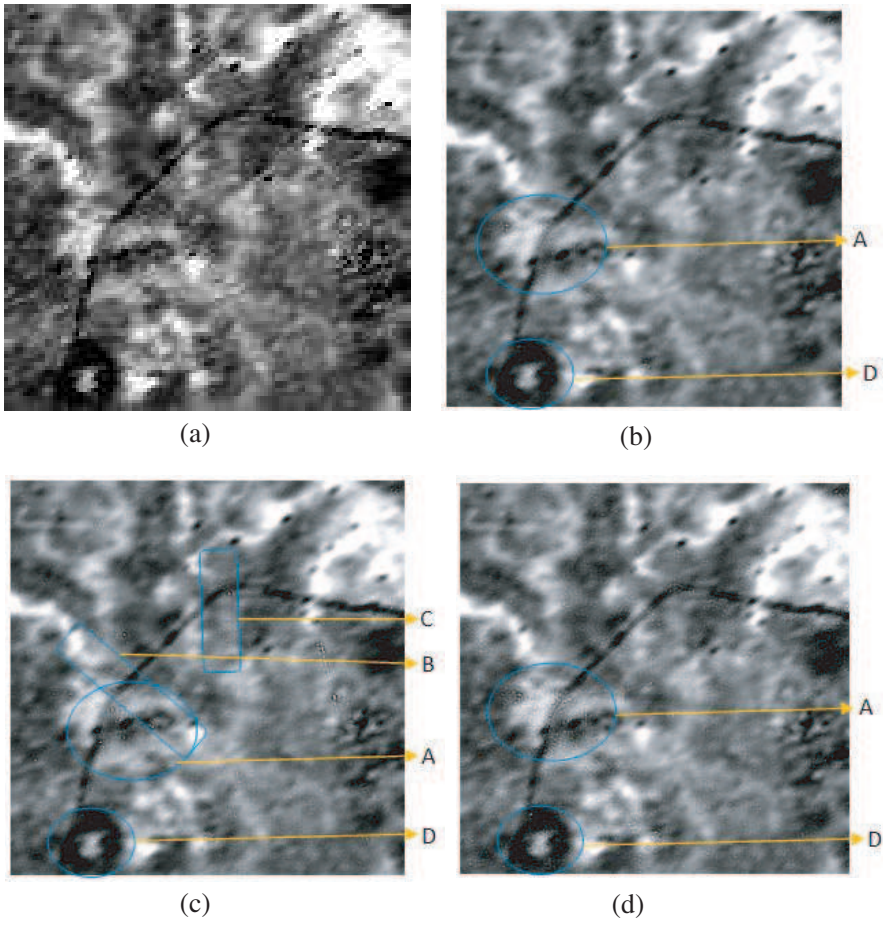

Figure 11. (a) MOD12, the resultant fused image of MODIS Band 1 and MODIS Band 2. (b) MO_PA(HH), the resultant fused image of MOD12 and HH polarized image. (c) MO_PA(HV), the resultant fused image of MOD12 and HV polarized image. (d) MO_PA(VV), the resultant fused image of MOD12 and VV polarized image.

MO1_PA(VV) (i.e., Figs. 9(a)–(c), 10(a)–(c), and 11(b)–(d) and it is marked in all the fused images by A. The D region is clearly shown in the fused images fused with MOD12, and MODIS Band 1, i.e., MO1_PA(HH), MO1_PA(HV), MO1_PA(VV), MO_PA(HH), MO_PA(HV) and MO_PA(VV) and is marked in Figs. 9(a), 9(b), 9(c), 11(b), 11(c) and 11(d).

This is not a very clear visual interpretation, but we can interfere

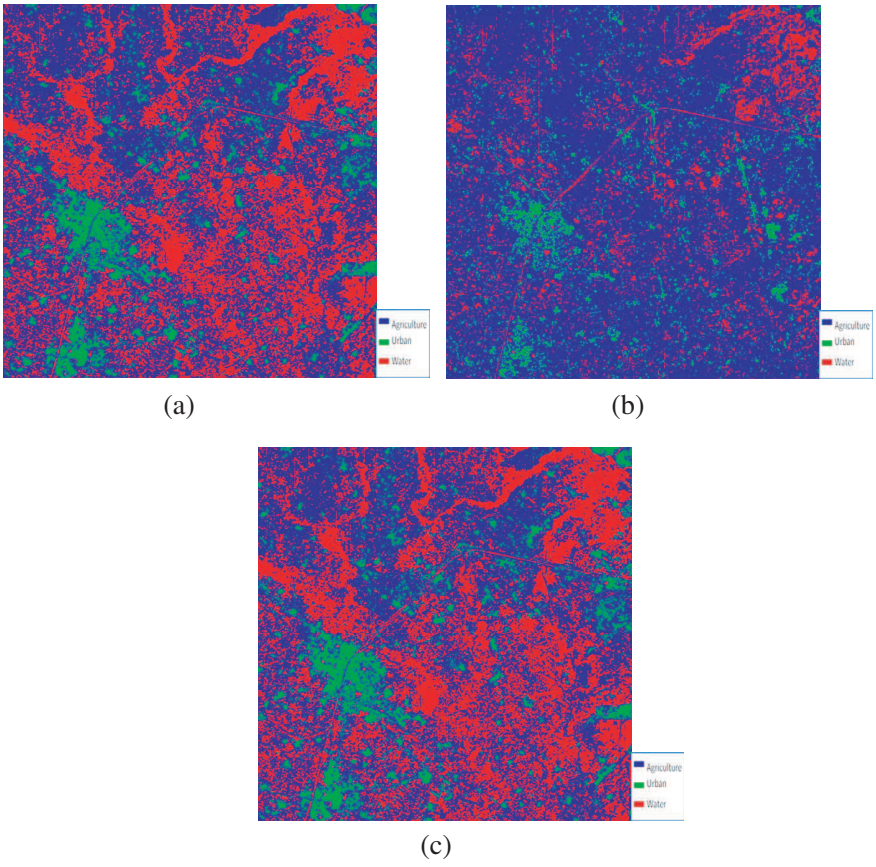

Figure 12. (a) Minimum distance classified PALSAR HH polarized. (b) Minimum distance classified PALSAR HV polarized. (c) Minimum distance classified PALSAR VV polarized.

that fusion of MODIS and PALSAR works and enhances some landcover. The fused image utility is checked by classification also which is presented in next section.

5.2. Classification Accuracy

The Minimum Distance classification technique has been applied for obtaining the major type of land cover classification, i.e., urban, agriculture and water. ENVI 4.3 software is used for georeferencing, calibration and classification purpose where as we have developed codes in MATLAB 7.0 for fusion methodology.

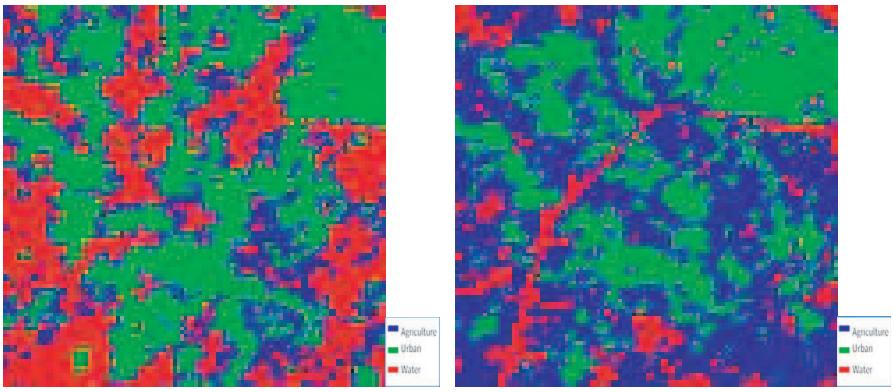

(a) (b)

Figure 13. (a) Minimum distance classified MODIS Band 1. (b) Minimum distance classified MODIS Band 2.

We have identified 392 Ground Control points (GCP) for agriculture, 358 GCP for urban and 311 GCP for water bodies for training and for testing 209 GCP for agriculture, 318 GCP for urban and 223 GCP for water bodies from Toposheet of Roorkee region which is shown in Fig. 6, Google earth, and Ground Survey points. The Control points were basically collected by ground survey with the use of GPS and more than 200 points were separately collected for each classes, and these points were overlapped on Google Earth and Toposheet for visual interpretation of the points. On the basis of these GCPs, we have computed the classification accuracy for PALSAR Bands.

Similarly for MODIS bands, we have identified 35 GCP for agriculture, 22 GCP for urban and 30 GCP for water bodies for training and for testing 38 GCP for agriculture, 27 GCP for urban and 28 GCP for water bodies and for the fused images, we have identified 355 GCP for agriculture, 309 GCP for urban and 333 GCP for water bodies for training and for testing 217 GCP for agriculture, 202 GCP for urban and 165 GCP for water bodies. On the basis of these GCPs, the Minimum Distance classification is calculated, and thereby classification accuracy is computed.

The minimum distance classified image of PALSAR HH, HV and VV Band are shown in Figs. 12(a), 12(b) and 12(c) respectively. In Figs. 13(a), 13(b), show the minimum distance classified image of MODIS Band 1 and Band 2. The minimum distance classified image of MO1_PA(HH), MO1_PA(HV) and MO1_PA(VV), the resultant

Table 1. Classification accuracy.

Images	Producers Accuracy			Users Accuracy			Overall Classification Accuracy
	Agriculture	Urban	Water	Agriculture	Urban	Water	
MODIS Band 1	23.68	44.44	82.14	42.86	48.00	48.94	47.3118
MODIS Band 2	63.16	48.15	92.86	60.00	54.17	89.66	67.7419
MOD12	39.47	59.26	82.14	57.69	53.33	62.16	58.0645
HH	28.71	79.87	82.06	36.59	100.0	55.12	66.2667
HV	58.85	96.23	95.07	84.25	100.0	71.14	85.4667
VV	31.58	80.50	74.44	35.68	100.0	53.72	65.0667
MO1_PA(HH)	82.95	76.73	75.15	68.18	100.0	75.15	78.5959
MO1_PA(HV)	82.49	73.76	75.15	66.79	100.0	74.25	77.3973
MO1_PA(VV)	82.03	76.24	75.15	66.92	99.35	76.07	78.0822
MO2_PA(HH)	88.02	54.95	95.15	66.55	82.84	96.32	78.5959
MO2_PA(HV)	89.86	58.91	95.76	70.14	85.00	95.18	80.8219
MO2_PA(VV)	86.64	55.94	94.55	66.67	82.48	94.55	78.2534
MO_PA(HH)	96.31	72.77	89.70	74.38	100.0	94.87	86.3014
MO_PA(HV)	94.47	71.29	88.48	72.70	100.0	92.41	84.7603
MO_PA(VV)	96.31	71.78	84.85	71.82	100.0	94.59	84.5890

fused image of MODIS Band 1 and PALSAR bands, is depicted in Figs. 14(a), 14(b) and 14(c) respectively. In Figs. 15(a), 15(b) and 15(c) shows the minimum distance classified image of MO2_PA(HH), MO2_PA(HV) and MO2_PA(VV) respectively, the resultant fused image of PALSAR (HH, HV and VV) and MODIS Band 2. The minimum distance classified image of MOD12, the resultant fused image of MODIS Band 1 and Band 2, is depicted in Fig. 16(a). The resultant fused image of MOD12 and PALSAR (HH, HV and VV) bands are MO_PA(HH), MO_PA(HV) and MO_PA(VV), and its minimum distance classified image is depicted in Figs. 16(b), 16(c) and 16(d) respectively.

The classification accuracy is calculated and tabulated in the Table 1. The fused image of MODIS Band 1 and PALSAR bands are MO1_PA(HH), MO1_PA(HV) and MO1_PA(VV), and there overall classification accuracy are 78.5959, 77.3973 and 78.0822 respectively. MO2_PA(HH), MO2_PA(HV) and MO2_PA(VV), the resultant fused image of MODIS Band 2 and PALSAR bands, and there overall classification accuracy are 78.5959, 80.8219 and 78.2534 respectively. The fused image of MOD12 and PALSAR bands are MO_PA(HH), MO_PA(HV) and MO_PA(VV), and there overall classification accuracy are 86.3014, 84.7603 and 84.5890 respectively. Thereby, the overall classification accuracy for the fused images with MOD12 is better that the overall classification accuracy for the fused

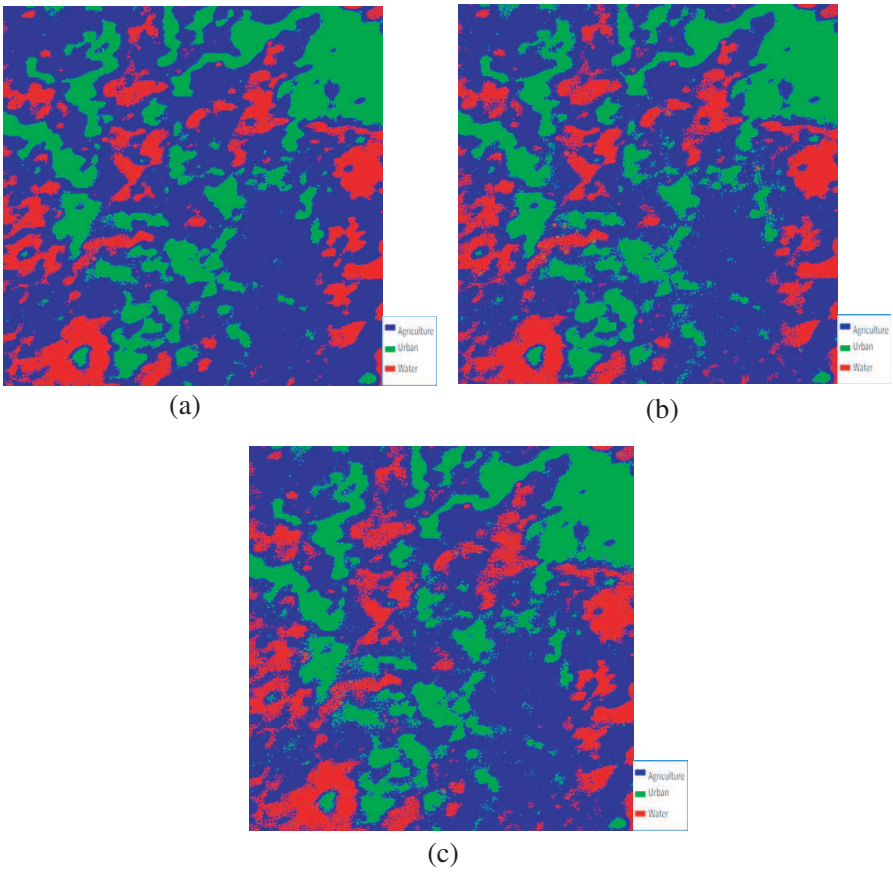

Figure 14. (a) Minimum distance classified MO1_PA(HH), the resultant fused image of MODIS Band 1 and HH Polarized image. (b) Minimum distance classified MO1_PA(HV), the resultant fused image of MODIS Band 1 and HV Polarized image. (c) Minimum distance classified MO1_PA(VV), the resultant fused image of MODIS Band 1 and VV Polarized image.

images with MODIS Band 2, and which is better than the overall classification accuracy for the fused images with MODIS Band 1.

The producers accuracy of agriculture for the fused image with MOD12, i.e., MO_PA(HH), MO_PA(HV) and MO_PA(VV) are 96.31, 94.47 and 96.31 respectively, and it is better than the producers accuracy of agriculture for the fused image with MODIS Band 2, i.e., MO2_PA(HH), MO2_PA(HV) and MO2_PA(VV) and there producers accuracy are 88.02, 89.86 and 86.64 respectively, and which is better than the producers accuracy of agriculture for the fused image with

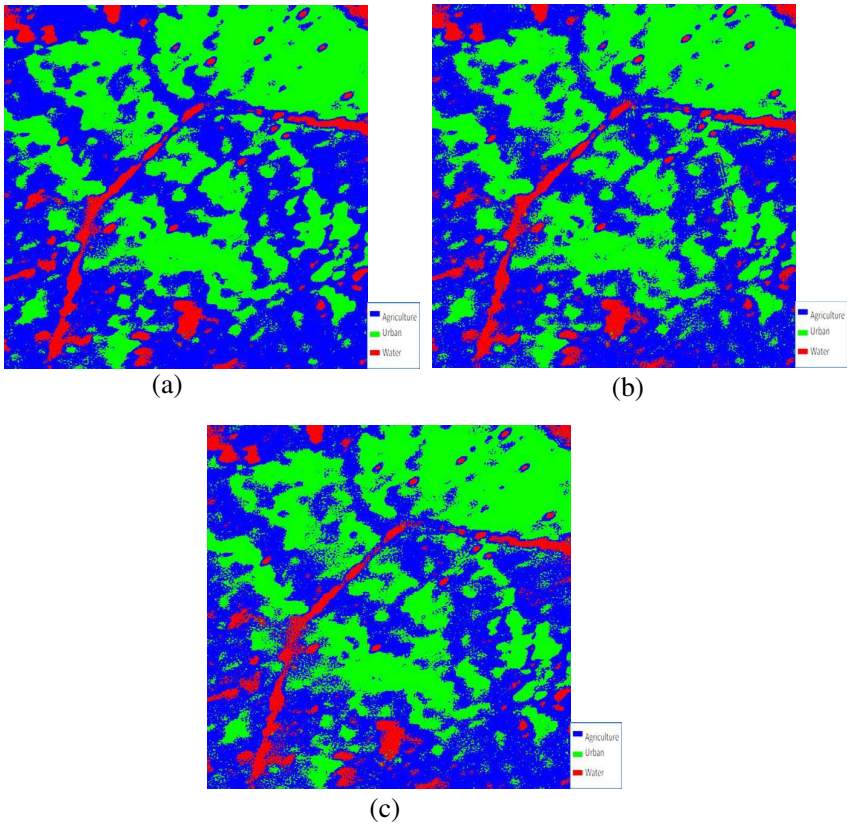

Figure 15. (a) Minimum distance classified MO2_PA(HH), the resultant fused image of MODIS Band 2 and HH Polarized image. (b) Minimum distance classified MO2_PA(HV), the resultant fused image of MODIS Band 2 and HV Polarized image. (c) Minimum distance classified MO2_PA(VV), the resultant fused image of MODIS Band 2 and VV Polarized image.

MODIS Band 1, i.e., MO1_PA(HH), MO1_PA(HV) and MO1_PA(VV) and there producers accuracy are 82.95, 82.49 and 82.03 respectively.

The producers accuracy of urban for the fused image with MODIS Band 1, i.e., MO1_PA(HH), MO1_PA(HV) and MO1_PA(VV) are 76.73, 73.76 and 76.24 respectively, and it is better than the producers accuracy of urban for the fused image with MOD12, i.e., MO_PA(HH), MO_PA(HV) and MO_PA(VV) and there producers accuracy are 72.77, 71.29 and 71.78 respectively, and which is better than the producers accuracy of urban for the fused image with MODIS

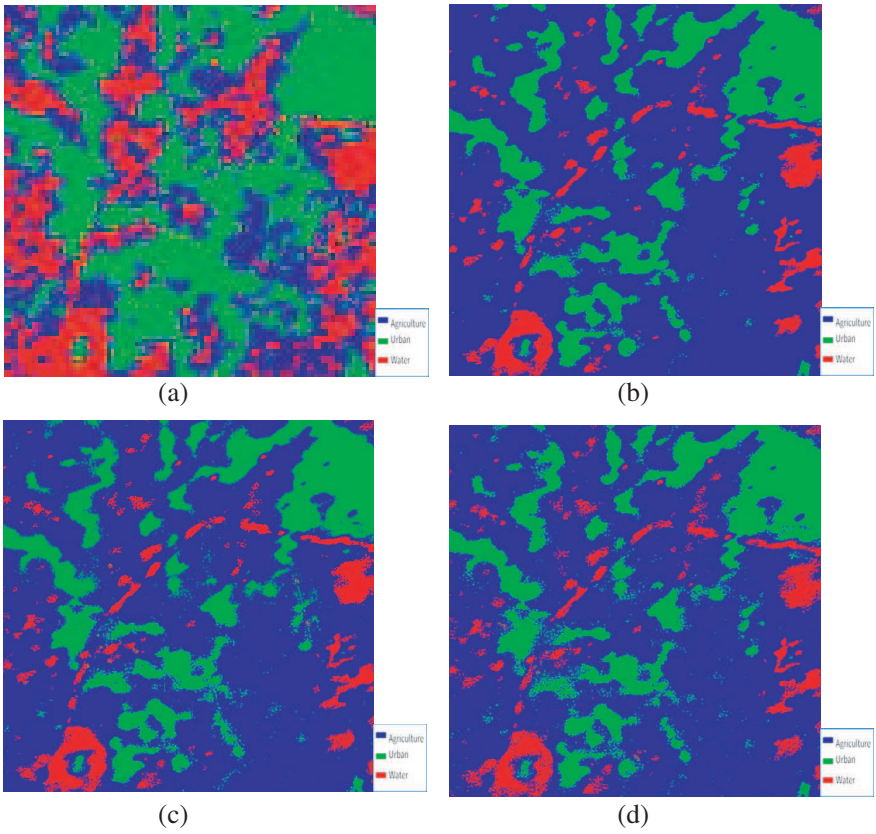

Figure 16. (a) Minimum distance classified MOD12 (resultant fused image of MODIS Band 1 and Band 2). (b) Minimum distance classified MO_PA(HH), the resultant fused image of MOD12 and HH Polarized image. (c) Minimum distance classified MO_PA(HV), the resultant fused image of MOD12 and HV Polarized image. (d) Minimum distance classified MO_PA(VV), the resultant fused image of MOD12 and VV Polarized image.

Band 2, i.e., MO2_PA(HH), MO2_PA(HV) and MO2_PA(VV) and there producers accuracy are 54.95, 58.91 and 55.94 respectively.

The producers accuracy of water for the fused image with MODIS Band 2, i.e., MO2_PA(HH), MO2_PA(HV) and MO2_PA(VV) are 95.15, 95.76 and 94.55 respectively, and it is better than the producers accuracy of water for the fused image with MOD12, i.e., MO_PA(HH), MO_PA(HV) and MO_PA(VV) and there producers accuracy are 89.70, 88.48 and 84.85 respectively, and which is better than the producers accuracy of water for the fused image with MODIS

Band 1, i.e., MO1_PA(HH), MO1_PA(HV) and MO1_PA(VV) and there producers accuracy are 75.15, 75.15 and 75.15 respectively.

The users accuracy of agriculture for the fused image with MOD12, i.e., MO_PA(HH), MO_PA(HV) and MO_PA(VV) are 74.38, 72.70 and 71.82 respectively, and it is better than the users accuracy of agriculture for the fused image with MODIS Band 2, i.e., MO2_PA(HH), MO2_PA(HV) and MO2_PA(VV) and there users accuracy are 66.55, 70.14 and 66.67 respectively, and which is better than the users accuracy of agriculture for the fused image with MODIS Band 1, i.e., MO1_PA(HH), MO1_PA(HV) and MO1_PA(VV) and there users accuracy are 68.18, 66.79 and 66.92 respectively.

The users accuracy of urban for the fused image with MOD12, i.e., MO_PA(HH), MO_PA(HV) and MO_PA(VV) are 100.00, 100.00 and 100.00 respectively, and it is better than the users accuracy of urban for the fused image with MODIS Band 1, i.e., MO1_PA(HH), MO1_PA(HV) and MO1_PA(VV) and there users accuracy are 100.00, 100.00 and 99.35 respectively, and which is better than the users accuracy of urban for the fused image with MODIS Band 2, i.e., MO2_PA(HH), MO2_PA(HV) and MO2_PA(VV) and there users accuracy are 82.84, 85.00 and 82.48 respectively.

The users accuracy of water for the fused image with MODIS Band 2, i.e., MO2_PA(HH), MO2_PA(HV) and MO2_PA(VV) are 96.32, 95.18 and 94.55 respectively, and it is better than the users accuracy of water for the fused image with MOD12, i.e., MO_PA(HH), MO_PA(HV) and MO_PA(VV) and there users accuracy are 94.87, 92.41 and 94.59 respectively, and which is better than the users accuracy of water for the fused image with MODIS Band 1, i.e., MO1_PA(HH), MO1_PA(HV) and MO1_PA(VV) and there users accuracy are 75.15, 74.25 and 76.07 respectively.

MO_PA(HH) the resultant image of fusion of MOD12 (Resultant image of MODIS Band 1 and Band 2) and HH PALSAR band is exemplifying the highest classification accuracy of 86.3014% overall classification accuracy comprising 96.31% of agriculture, 72.77% of water and 89.70% of urban producers accuracy, and 74.38% of agriculture, 100.0% of water and 94.87% of urban users accuracy.

5.3. Quality Assessment

The correlation coefficient, RMSE, RMD, RVD, DI, PSNR and UQI is computed as by the (11), (12), (13), (14), (15), (16), (16) and (17) respectively. These quality assessment indicators have been calculated for the fused images, with respect to MODIS Bands. In Table 2, the quality assessment indicators are tabulated for the fused images MO1_PA(HH), MO1_PA(HV), MO1_PA(VV), with respect to MODIS

Table 2. Quality assessment indicators between MODIS Band 1 and PALSAR Bands.

	MODIS Band 1						
	Corr	**RMSE**	**RMD**	**RVD**	**DI**	**PSNR**	**UQI**
MO1_PA(HH)	0.9917	4.0861	–0.3044	–0.6249	0.2965	16.6188	0.0080
MO1_PA(HV)	0.9802	6.3747	–0.2434	–0.5399	0.3691	16.5318	0.0060
MO1_PA(VV)	0.9722	7.6103	–0.1974	–0.5933	0.3222	19.4116	0.0072

Table 3. Quality assessment indicators between MODIS Band 2 and PALSAR Bands.

	MODIS Band 2						
	Corr	**RMSE**	**RMD**	**RVD**	**DI**	**PSNR**	**UQI**
MO2_PA(HH)	0.9838	4.0841	–0.2739	–0.5428	0.1932	16.2280	0.0078
MO2_PA(HV)	0.9620	6.3744	–0.2758	–0.5174	0.2748	14.8443	0.0062
MO2_PA(VV)	0.9471	7.6093	–0.1917	–0.5070	0.3036	15.9705	0.0075

Table 4. Quality assessment indicators between MOD12 (MODIS Band 1 + Band 2) and PALSAR Bands.

	MOD12						
	Corr	**RMSE**	**RMD**	**RVD**	**DI**	**PSNR**	**UQI**
MO_PA(HH)	0.9920	4.0749	–0.3717	–0.6388	0.1896	20.8267	0.0118
MO_PA(HV)	0.9807	6.3681	–0.3246	–0.5753	0.2373	17.9525	0.0106
MO_PA(VV)	0.9728	7.6042	–0.3098	–0.6250	0.2724	19.7172	0.0104

Band 1. The quality assessment indicators for the fused images MO2_PA(HH), MO2_PA(HV), MO2_PA(VV) with respect to MODIS Band 2 is tabulated in the Table 3. And in Table 4 the quality assessment indicators are tabulated for the fused images MO_PA(HH), MO_PA(HV), MO_PA(VV) with respect to MOD12 (Resultant fused image of MODIS Band 1 and Band 2).

There exists a high closeness between MOD12 and MO_PA(HH), as the correlation indicator has the highest value, from the Tables 2, 3, 4. The degree of change is least between MO_PA(HH) and MOD12, as the RMSE is low. The fused image which will best preserve the spectral information is the one that has the smallest possible RMD, and from the Table 2, 3, 4, the smallest possible RMD exists between MO_PA(HH) and MOD12. The RVD between MO_PA(HH) and MOD12 is low, and hence it implies, the RVD of MO_PA(HH)

and MOD12 preserves the best spectral information. The fused image which will best preserve the spectral information is the one that has the smallest possible DI, and the DI of MO_PA(HH) and MOD12 is low, and thereby the spectral information is preserved. The PSNR between MO_PA(HH) and MOD12 is high, and hence it implies, the PSNR of MO_PA(HH) and MOD12 preserves the best spectral information. The fused image which will best preserve the spectral information is the one that has the highest possible UQI, and the UQI of MO_PA(HH) and MOD12 is high, and thereby the high spectral information is preserved.

Above discussions implies that the quality assessment indicators like correlation coefficient, RMSE, RMD, RVD, DI, PSNR and UQI produce a better fused result for MO_PA(HH) (i.e., resultant fused image of MOD12 and HH).

6. CONCLUSION

A curvelet transform based fusion is applied to various combination of PALSAR with MODIS image to assess the quality of fused image. The fused images are visually and quantitatively analyzed by quality assessment indicators (Correlation Coefficient, Root Mean squared error, Relative Mean Difference, Relative Variation Difference, Deviation Index, Peak signal-to-noise ratio (PSNR), Universal Image Quality Index) in one hand, and in another hand land cover classification accuracy is also compared with fused and without fused image. It is clearly observed that the resultant fused image of HH-PALSAR image with MOD12 (Resultant fused image of MODIS Band 1 and Band 2), i.e., MO_PA(HH), is providing maximum classification accuracy in comparison to other combinations of fused images. It is evident that the overall classification accuracy of fused image is quite enhanced in comparison to the classification accuracy of individual MODIS images, i.e., MODIS Band 1 and MODIS Band 2. It is inferred with the quality indicators that the fused images are preserving their spectral behavior but enhancing the spatial information as it is clear from the results of classification accuracies. This type of fusion may be helpful in near future to maximize the use of MODIS images.

ACKNOWLEDGMENT

Authors are thankful to Department of Science and Technology, India for providing the financial support for this work.

REFERENCES

1. Pohl, C. and J. L. van Genderen, "Multisensor image fusion in remote sensing: Concepts, methods, and applications," *International Journal of Remote Sensing*, Vol. 19, No. 5, 823–854, 1998.
2. Shen, S. S., "Summary of types of data fusion methods utilized in workshop papers," *Proceedings of Multisource Data Integration in Remote Sensing Workshop*, 145–149, NASA Conference Publication 3099, Greenbelt, Maryland, June 14–15, 1990.
3. Brisco, B. and R. J. Brown, "Multidate SAR/TM synergism for crop classification in western Canada," *Photogrammetric Engineering and Remote Sensing*, Vol. 61, No. 7, 1009–1014, 1995.
4. Harris, J. R., R. Murray, and T. Hirose, "IHS transform for the integration of radar imagery and other remotely sensed data," *Photogrammetric Engineering and Remote Sensing*, Vol. 56, No. 11, 1631–1641, 1990.
5. Raghavawamy, V., N. C. Gautam, M. Padmavathi, and K. V. S. Badarinath, "Studies on microwave remote sensing data in conjunction with optical data for land use/land cover mapping and assessment," *Geocarto International*, Vol. 11, No. 4, 25–31, 1996.
6. Welch, R. and M. Ehlers, "Cartographic feature extraction with integrated SIR-B and Landsat TM images," *International Journal of Remote Sensing*, Vol. 9, No. 5, 873–889, 1988.
7. Richards, J. A. and X. Jia, *Remote Sensing Digital Image Analysis — An Introduction*, 4th Edition, Springer, 2005.
8. Alparone, L., S. Baronti, A. Garzelli, and F. Nencini, "Landsat ETM+ and SAR image fusion based on generalized intensity modulation," *IEEE Transactions on Geoscience and Remote Sensing*, Vol. 42, No. 11, 2832–2839, 2004.
9. Amarsaikhan, D. and T. Douglas, "Data fusion and multisource image classification," *International Journal of Remote Sensing*, Vol. 25, No. 14, 3529–3539, 2004.
10. Hegarat-Mascle, S. L., A. Quesney, D. Vidal-Madjar, O. Taconet, M. Normand, and C. Loumagne, "Land cover discrimination from multitemporal ERS images and multispectral Landsat images: A study case in an agricultural area in France," *International Journal of Remote Sensing*, Vol. 21, 435–456, 2000.
11. Edwards, K. and P. A. Davis, "The use of Intensity-Hue-Saturation transformation for producing color shaded-relief images," *Photogramm. Eng. Remote Sens.*, Vol. 60, No. 11, 1369–

1374, 1994.

12. Schetselaar, E. M., "Fusion by the IHS transform: Should we use cylindrical or spherical coordinates?" *Int. J. Remote Sens.*, Vol. 19, No. 4, 759–765, 1998.
13. Gillespie, A. R., A. B. Kahle, and R. E. Walker, "Color enhancement of highly correlated images — II. Channel ratio and 'chromaticity' transformation techniques," *Remote Sens. Environ.*, Vol. 22, 343–365, 1987.
14. Zhou, J., D. L. Civco, and J. A. Silander, "A wavelet transform method to merge Landsat TM and SPOT panchromatic data," *Int. J. Remote Sens.*, Vol. 19, No. 4, 743–757, 1998.
15. Chavez, P. S. and A. Y. Kwarteng, "Extracting spectral contrast in Landsat Thematic Mapper image data using selective principle component analysis," *Photogramm. Eng. Remote Sens.*, Vol. 55, No. 3, 339–348, 1989.
16. Pajares, G. and J. M. de la Cruz, *A Wavelet-based Image Fusion Tutorial*, Pattern Recognition 37, 1855–1872, Elsevier Ltd, 2004.
17. Yocky, D. A., "Artifacts in wavelet image merging," *Optical Engineering*, Vol. 35, No. 6, 2094–2101, 1996.
18. Gonzáles Audícana, M., J. L. Saleta, R. García Catalán, and R. García, "Fusion of multispectral and panchromatic images using improved IHS and PCA mergers based on wavelet decomposition," *IEEE Transactions on Geoscience and Remote Sensing*, Vol. 42, No. 6, 1291–1299, 2004.
19. Starck, J. L., E. J. Candès, and D. L. Donoho, "The curvelet transform for image denoising," *IEEE Trans. Image Processing*, Vol. 11, 670–684, 2002.
20. Do, M. N. and M. Vetterli, "The finite ridgelet transform for image representation," *IEEE Transactions on Image Processing*, Vol. 12, No. 1, 16–28, 2003.
21. Justice, C. O., E. Vermote, J. G. R. Townshend, et al., "The Moderate Resolution Imaging Spectroradiometer (MODIS): Land remote sensing for global change research," *IEEE Transactions on Geoscience and Remote Sensing*, Vol. 36, 1228–1249, 1998.
22. Rosenqvist, A., M. Shimada, N. Ito, and M. Watanabe, "ALOS PALSAR: A pathfinder mission for global-scale monitoring of the environment," *IEEE Transactions on Geoscience and Remote Sensing*, Vol. 45, 3307–3316, 2007.
23. Shensa, M. J., "The discrete wavelet transform: Wedding the à trous and Mallat algoritm," *IEEE Trans. Signal Process.*, Vol. 40, No. 9, 2464–2482, 1992.

24. Filippo, N., A. Garzelli, S. Baronti, and L. Alparone, "Remote sensing image fusion using the curvelet transform," *Information Fusion*, Vol. 8, 143–156, 2007.
25. Choi, M., R. Y. Kim, and M. G. Kim, "The curvelet transform for image fusion," *International Society for Photogrammetry and Remote Sensing, ISPRS 2004*, Vol. 35, Part B8, 59–64, Istanbul, 2004.
26. Choi, M., R. Y. Kim, M. R. Nam, and H. O. Kim, "Fusion of multispectral and panchromatic satellite images using the curvelet transform," *IEEE Geosci. Remote Sensing Lett.*, Vol. 2, No. 2, 136–140, 2005.
27. Wald, L., T. Ranchin, and M. Mangolini, "Fusion of satellite images of different spatial resolutions: Assessing the quality of resulting images," *Photogramm. Eng. Remote Sens.*, Vol. 63, No. 5, 691–699, 1997.
28. Acerbi-Junior, F. W., J. G. P. W. Clevers, and M. E. Schaepman, "The assessment of multi-sensor image fusion using wavelet transforms for mapping the Brazilian Savanna," *International Journal of Applied Earth Observation and Geoinformation*, Vol. 8, 278–288, 2006.
29. Vijayaraj, V., N. H. Younan, and C. G. O'Hara, "Quality metrics for multispectral image processing," *Proceedings of the Annual ASPRS Conference*, 2004.
30. Karathanassi, V., P. Kolokousis, and S. Ioannidou, "A comparison study on fusion methods using evaluation indicators," *International Journal of Remote Sensing*, Vol. 28, No. 9, 2309–2341, 2007.
31. Li, S., J. T. Kwok, and Y. Wang, "Using the discrete wavelet frame transform to merge Landsat TM and SPOT panchromatic images," *Information Fusion*, Vol. 3, 17–23, 2002.
32. De Bethune, S., F. Muller, and J.-P. Donnay, "Fusion of multispectral and panchromatic images by local mean and variance matching filtering techniques," *Proceedings of Fusion of Earth Data*, 31–37, National Remote Sensing Agency, Hyerabad, 1998.
33. Li, Q. and Q. Hu, "3D wavelet compression to multiple band remote sensing images based on edge reservation," *Proceedings of the ISPRS, Commission VII*, No. 11, Istanbul, 2004.
34. Wang, Z. and A. C. Bovic, "A universal image quality index," *IEEE Signal Processing Letters*, Vol. 9, 81–84, 2002.
35. SARSCAPE help document (provided by SARSCAPE).